

Shahfiq Shahjahan<sup>1</sup> & Dries Verstraete<sup>1</sup>

<sup>1</sup>The University of Sydney, NSW 2006, Australia

#### **Abstract**

Proprotor designs often overlook the consideration of the vehicle's motor powertrain. This paper introduces an optimisation method that explicitly accounts for the coupling with the vehicle's powertrain. Proprotors are optimised for an electric Vertical Take-off and Landing (eVTOL) vehicle under nominal cruise, hover, and one-motor hover conditions, employing three distinct electric motors with the same power rating but different maximum torque and rotational speed characteristics. Results indicate that the Pareto-optimal proprotor designs are significantly influenced by the specific powertrain to which they are coupled. Proprotors designed with higher maximum torque and lower maximum rotational speed exhibit larger chord and pitch distributions compared to proprotors designed with lower maximum torque and higher maximum rotational speed.

Keywords: Advanced Air Mobility; Edgewise Flight; eVTOL; Optimisation; Proprotor

## 1. Introduction

Scale-free distributed electric propulsion (DEP) opens up a more extensive vehicle design space and enables new aircraft concepts [1]. A vertical take-off and landing transitioning aircraft can benefit the most from DEP due to the significant mismatch of power requirements between take-off and cruise [2]. An aircraft capable of taking off and landing like a rotorcraft, with the same efficiency as a fixed-wing aircraft in terms of the speed, range, endurance, and load-carrying capability, is called a transitioning aircraft [3]. Interest in the use of electric Vertical Take-off and Landing (eVTOL) aircraft for use as air taxis or for medical evacuation services has increased recently [4–8]. On a smaller scale, they are increasingly used for a variety of reconnaissance, and remote-sensing missions, aerial photography, environmental monitoring, disaster relief, and search and rescue operations [9–18]. The design freedom offered by scale-free DEP and the need to balance the efficiency in hover and cruise has resulted in a wide range of eVTOL configurations [19–21], which can broadly be classified into three main categories: wingless, lift+cruise, and vectored thrust. Designs in each category face unique challenges and aero-propulsive interactions.

The main focus of this study is on the vectored thrust category eVTOLs. Proprotors, which act as rotors during vertical flight and propellers during forward flight, are typically employed for the eVTOL category. A well-designed proprotor for tilt-wing aircraft should operate efficiently in all flight conditions exhibiting high figure-of-merit at hover and high propeller efficiency at cruise. Designing proprotors raises unique challenges as they not only operate at two very different flight conditions (typically cruise and hover), the aircraft's propulsion system also needs to work efficiently between two very different power levels [22].

The conventional approach to propeller design often isolates the propeller's design from the vehicle's powertrain [23–25]. However, this seemingly straightforward strategy can lead to significant declines in overall vehicle performance if the propeller and powertrain are not matched. After all, the propulsion system's overall efficiency combines both the propeller and powertrain efficiencies [26]. Therefore, an optimal propeller design should transcend considerations of aerodynamic performance

and structural constraints. It necessitates a comprehensive understanding of the interplay between the propeller and the powertrain at various operational points [9, 26]. Considering both propeller and powertrain efficiencies ensures that the propeller is precisely tailored to complement the specific operational requirements and capabilities of the coupled powertrain, ultimately enhancing overall vehicle performance. This study outlines the influence of the powertrain motor map to the final shape of the optimised proprotors.

The remainder of this paper is organised as follows. The methodology section describes the aerodynamic, acoustic, structural, and electric motor models used in this study. The following section then outlines the optimisation problem, such as design variables and constraints associated with proprotor optimisation and introduces the optimisation algorithm. Next, the operating conditions and objectives are explained alongside the results and discussions of executed optimisation cases. The conclusion section then highlights the main outcomes of the study.

# 2. Methodology

Our multidisciplinary optimisation framework combines an aerodynamic, an acoustic, a structural, and an electric motor model. As optimisation requires many function calls, each analysis model must be computationally efficient and sufficiently accurate.

# 2.1 Aerodynamic Model

Blade Element Momentum Theory (BEMT) is widely embraced in propeller design, especially within optimisation, for its computational efficiency [9, 26–31]. In this study, an extended BEMT method, informed by MacNeill and Verstraete [32] is used. This extended model incorporates enhancements such as expanding the aerodynamic database to include high angles of attack, through the Viterna-Corrigan flat plate theory [33]. Additionally, it considers the effects of rotation using the correction method proposed by Snel et al. [34]. For a more comprehensive understanding and validation of the extended BEMT method, readers are directed to the detailed description in ref. [31, 32].

We have extensively validated our integration of the aerodynamic database [31], obtained here from XFOIL [35], with BEMT with known experimental data for a range of propellers such as the APC10x5 thin electric propeller [36], V-22 rotor [37] and Rabbott rotor [38]. The BEMT results show good agreement with experimental data across most operating conditions, although some discrepancies occur at low advance ratios. We obtain a maximum error of 11% on both thrust and power coefficients. The detailed validation study can be found in ref. [31].

In conditions of edgewise or transition flight, the rotor operates with its disk at a non-zero angle of attack relative to the freestream velocity  $\alpha_p$ . To address the oblique incoming flow, we enhance the BEMT by incorporating the non-uniform induced velocity model developed by Leishman [39]:

$$\lambda_i = \lambda_0 \left( 1 + k_{\chi} r \cos(\psi) + k_{\nu} r \sin(\psi) \right) \tag{1}$$

Here,  $\lambda_i$  denotes the non-dimensionalised inflow factor,  $\psi$  represents the azimuthal location of the blade element in the rotor disk, and  $k_\chi$  and  $k_\chi$  serve as the weighting coefficients for the linear distribution of induced flow. Equation 1 is solved iteratively, with the study adopting the weighting coefficients proposed by Drees [40]:

$$k_{\chi} = \frac{4}{3} \left( \frac{1 - \cos(\chi) - 1.8J_t^2}{\sin(\chi)} \right)$$

$$k_{\nu} = -2J_t$$
(2)

where  $\chi=\tan^{-1}\left(\frac{J_t}{J_a'+\lambda_i}\right)$  signifies the wake skew angle,  $J_t=\frac{V_{\infty}\sin(\alpha_p)}{\Omega R}$  denotes the tangential advance ratio, and  $J_a'=\frac{V_{\infty}\cos(\alpha_p)}{\Omega R}$  represents the inflow advance ratio.

The extended BEMT method, incorporating the non-uniform inflow model, is validated against experimental results from Serrano et al. [41] on the APC Sport 12x6 propeller under oblique flow. The detailed validation study for propeller operating in edgewise flight can be found in ref. [31].

## 2.2 Acoustic Model

Rotor noise comprises two primary components: loading noise, stemming from thrust production, and thickness noise, arising from finite rotor blade thickness [1]. The resulting noise can be represented by Equations 3 and 4 [42, 43]:

$$p_{m_L} = \frac{mB\Omega}{2\sqrt{2}\pi a \left(\Delta S\right)} \int_{hub}^{tip} \left[ \frac{dT}{dr} \cos\theta - \frac{dQ}{dr} \frac{a}{\Omega r^2} \right] J_{mB} \left( \frac{mB\Omega}{a} r \sin\theta \right) dr \tag{3}$$

$$p_{m_T} = \frac{-\rho (mB\Omega)^2 B}{3\sqrt{2}\pi (\Delta S)} \int_{hub}^{tip} ct J_{mB} \left(\frac{mB\Omega}{a} r \sin \theta\right) dr \tag{4}$$

where  $p_{m_L}$  and  $p_{m_T}$  denote the sound pressure for loading and thickness noise, respectively. The variables include m for the harmonic number, B for the number of rotor blades,  $\Omega$  for the rotor rotation rate, a for the speed of sound, and  $\Delta S$  for the distance between the rotor and the observer. Additionally, T represents the thrust produced, Q is the rotor torque, r signifies the rotor radial location,  $\theta$  stands for the observer's azimuthal location,  $\rho$  represents air density, c is the blade chord, t denotes the blade maximum thickness, and  $J_{mB}$  is a Bessel function of the first kind with order mB. Despite the existence of more accurate models, we opt for the computational efficiency of the simplified models in Equations 3 and 4, aligning well with their application in an optimisation framework. As detailed in ref. [31], the model is able to predict the noise production within 5% of experimental measurement.

## 2.3 Structural Model

A non-linear finite element analysis (FEA) slender beam model, as detailed in [44], serves to capture the structural behavior of the blade. Adopting a box-beam spar structure (Figure 1), we presume that the internal loads are fully borne by this spar. For the optimisation process, the width w and thicknesses  $t_x$  and  $t_z$  of the box beam are chosen as the structural design variables. The validity of a similar structural model has been established in prior work [31, 45].

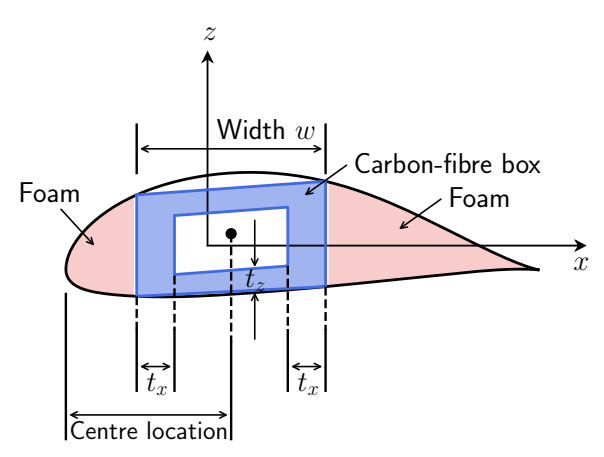


Figure 1 – Internal structure of the propeller

The internal structure comprises two materials: Hexcell AS4-3501-6 Carbon Fiber/Epoxy Pre-preg for the box-beam spar and aerospace-grade foam (Evonik ROHACELL) to maintain the blade section's shape. We use material properties of these components from ref. [46–50].

To ensure the spar's load-bearing capability at each blade section [45], bending stresses are computed, considering the centrifugal force from the blade's rotation [26]. The resultant combined loading at each section is transformed to determine the principal stresses around the section. These principal stresses, in turn, contribute to the evaluation of the failure criterion, with their values aggregated

across each blade section using the Kreisselmeier-Steinhauser (KS) method [51]. The application of the KS constraint aggregation enables a single value to quantify the 'level' of stress violation or structural failure across the blade geometry.

## 2.4 Electric Motor Model

To ensure effective matching between the motor and proprotor, we consider the entire powertrain, including the electric motor and we use the electric motor model developed by Drela [52] to generate representative motor operating maps. This motor model variations in motor losses with rotational speed and torque. The equation describing the motor model to give current (i), shaft torque ( $Q_m$ ), power ( $P_{shaft}$ ) and motor efficiency ( $\eta_m$ ), with each parameter a function of motor rotational speed ( $\Omega$ ) and terminal voltage ( $\nu$ ) [52]:

$$\eta_m(\Omega, v) = \frac{P_{shaft}}{iv} = \left(1 - \frac{i}{i_0}\right) \frac{K_V}{K_Q} \frac{1}{1 + iRK_V/\Omega}$$
(5)

where  $i_0$  is the no-load current,  $K_V$  is the speed constant,  $K_Q$  is the torque constant and R is the motor resistance. With the above model, the motor map of any electric motor can be modelled if the first order constant  $(i_0, K_V, i_0, R)$  are known.

The motor map employed in this study, depicted in Figure 2, is based on publicly available data for the Geiger Engineering HPD50D electric motor [53]. For the present investigation, we specifically explore the ifluence of the motor map on the optimised proprotor. Consequently, two motor maps are considered: 1) the original motor map, 2) a second motor map where we increase the torque to a peak torque of 175 Nm, and 3) a third motor map where we double the torque to a peak torque of 250 Nm while adjusting the maximum rotational speed to maintain a constant maximum available power.

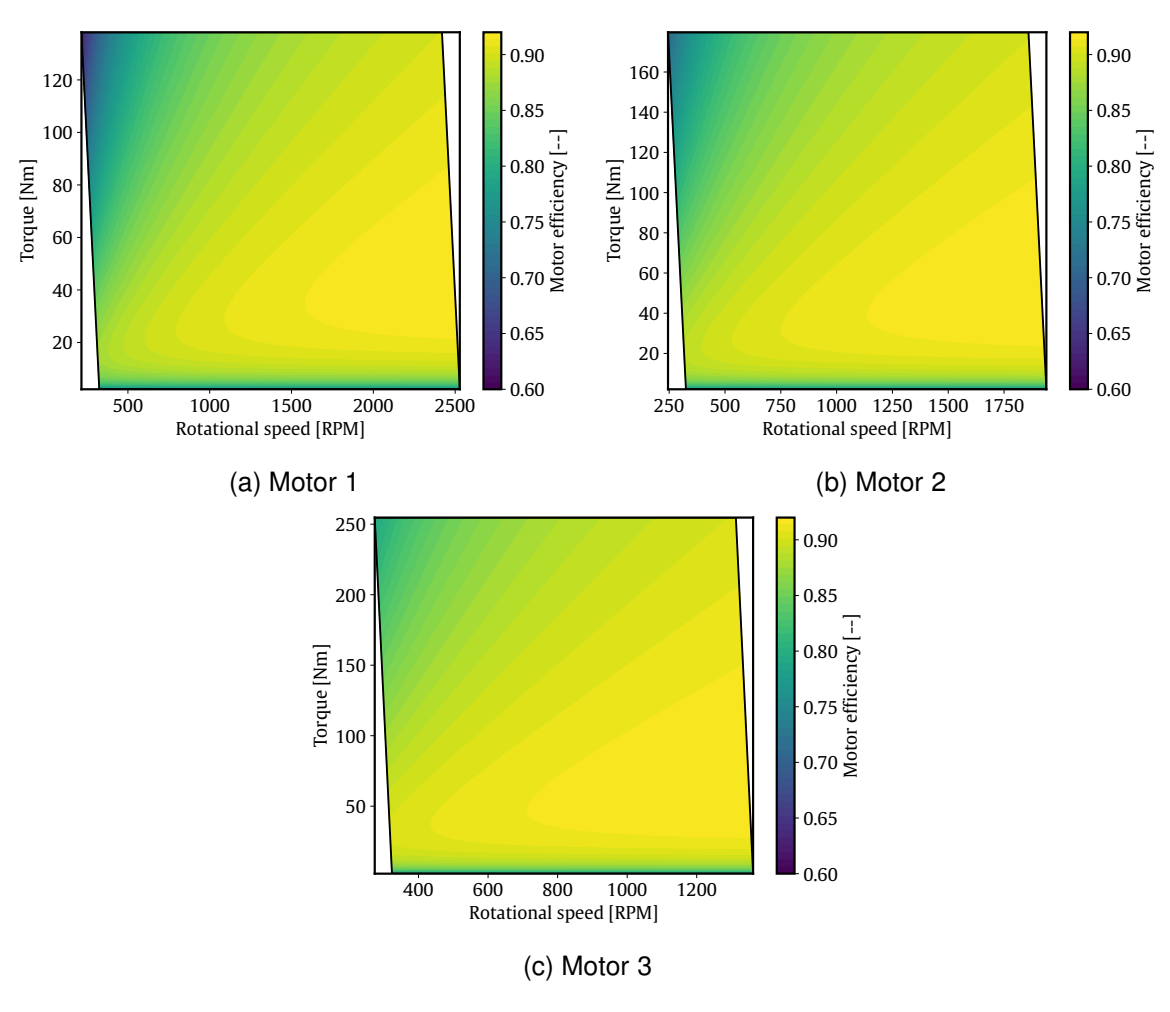


Figure 2 - Electric motor map

# 3. Proprotor Optimisation

This section outlines the optimisation problem, including design variables and constraints, and the optimisation algorithm used in this study. We consider 31 variables with 14 constraints and 4 objectives for the various problems reported here.

# 3.1 Design Variables

We classify the design variables into three primary groups: planform design variables, structural design variables, and operational design variables. The structural design variables are described in Section 2.3, whereas the planform and operational design variables are detailed next.

For the planform design variables, we employ fourteen parameters to represent the chord (c) and the pitch angle distribution  $(\beta)$  of the proprotor. Both distributions are defined through a Bezier spline based on seven uniformly distributed control points along the blade span, where the root of the blade is positioned at a radial coordinate of  $r/R = 0.115^{1}$ . The Bezier parametrisation ensures continuity across the blade, and wide bounds are intentionally set for both chord and pitch control points to enable exploration of a large design space (Figure 3).

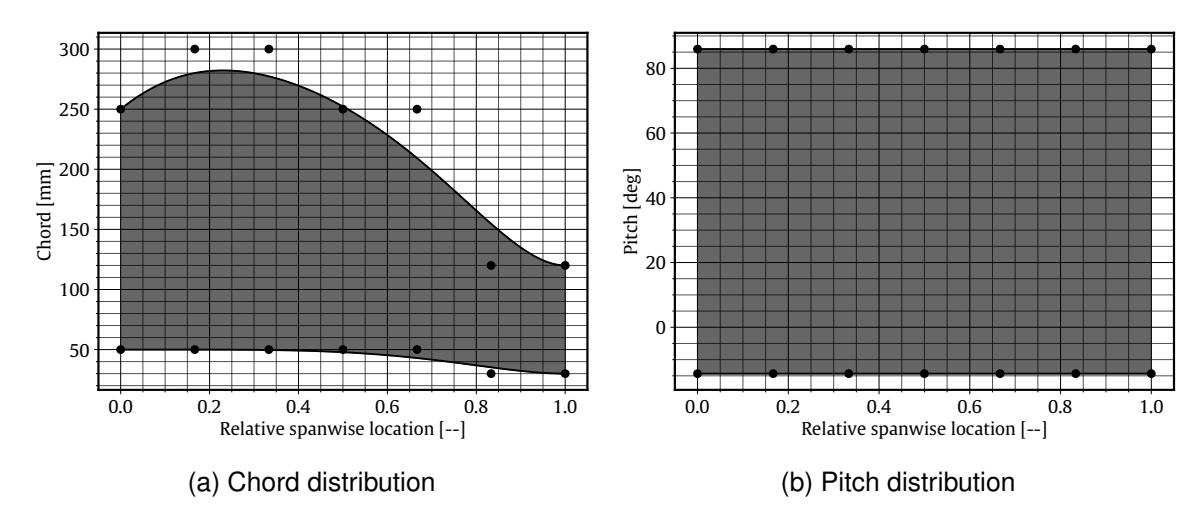


Figure 3 – Chord and pitch design variable bounds (● is the control point and the shaded region is the bounding box)

To fully characterise the proprotor blade shape, we also specify airfoils at ten radial locations along the blade. Airfoil selection is treated as a discrete variable, allowing the optimiser to choose from a fixed set of nine airfoils (MH series propeller airfoils [54]) with thickness-to-chord ratios (t/c) ranging from 8.76% to 25%.

The number of propeller blades  $(n_b)$  and the propeller radius (R) are not considered as design variables but are fixed at 3 blades and 0.95 m, respectively [55].

For each flight condition, operational design variables, such as rotational speed, are introduced. The design variables and their corresponding lower and upper bounds are summarised in Table 1.

## 3.2 Constraints

To guarantee the viability of the proprotor designs, we enforce several constraints. For each operating condition, we implement constraints on minimum thrust, powertrain torque, and stress violation. Aligning with the criteria outlined by Uber Elevate [1], we additionally impose a noise constraint of 62 dB for hovering at 500 ft altitude. In total, we establish  $2+3n_{fc}$  constraints, where  $n_{fc}$  denotes the number of flight conditions.

<sup>&</sup>lt;sup>1</sup>We locate the root of the blade at a radial position r/R = 0.115. Thus, the control points are defined as  $r/R : 0.115 \rightarrow 1$ ,  $y: 0 \rightarrow 1$ .

Table 1 – Overview of the design variables

Design Parameter	No. of Variables	Bou Lower	inds Upper
Airfoil Selection	10	N/A	
Chord (c) Pitch (β)	7 7	See Figure 3a See Figure 3b	
Box-beam Width-to-Chord Box-beam $t_x$ -to-Width Box-beam $t_z$ -to-Height	1 1 1	0.3 0.1 0.1	0.5 0.35 0.35
Rotation Rate [RPM]	4	See Figure 2	

# 3.3 Optimisation Algorithm

While our optimisation setup is algorithm agnostic, we use the SHAMODE-WO algorithm [56], driven by its demonstrated competitive performance in our preliminary investigations. The Success History-based Adaptive Multi-Objective Differential Evolution (SHAMODE) algorithm integrates a differential evolution (DE) offspring generation mechanism with an additional mutation and crossover operator [56]. To expedite convergence, the scaling factor of the DE offspring generation and the crossover ratio dynamically adapt based on a historical memory. The comprehensive details on the SHAMODE-WO algorithm can be found in ref. [56].

Although the original SHAMODE-WO algorithm uses the feasible-first mechanism for survival, [56] we opt for NSGA-III's reference direction survival mechanism [57, 58]. This choice is motivated by the observation that, in scenarios with many objectives, the ranking-based survival mechanism of NSGA-III introduces a more lenient selection pressure [57, 58].

# 4. Optimisation of a Proprotor for Electric Vertical Take-off and Landing aircraft

We apply the optimisation procedure to a eVTOL aircraft that is loosely modelled after the Skyfly Axe. Our Skyfly Axe-like eVTOL aircraft has a wing and canard span of 5.0 m, a maximum take-off weight of 652 kg, and is equipped with eight brushless motors, featuring two per wing end [55]. The two motors are in a single housing, both driving a common shaft, ensuring redundancy in the motor unit. The aircraft geometry and characteristics are shown and summarised in Figure 4 and Table 2.



Figure 4 – Geometry of Skyfly Axe-like tilt-wing eVTOL aircraft [55]

We run three series of optimisation cases. The first series is with the original motor (Motor 1), while the second and third with the modified motor (Motor 2 and Motor 3). The operating conditions used in both series are described next.

# 4.1 Operating Conditions and Objectives

In this study, four different flight conditions are considered. The first operating condition is the aircraft's nominal cruise condition, for which we use a flight speed of 44.7 m/s at 500 m altitude [55]. In cruise, the proprotor is operating at an inclination angle of 45° relative to the freestream velocity. The second and third operating conditions represent a sustained (nominal) hover, and emergency hover condition at an altitude of 25 m. The emergency hover condition ensures that the propulsion system of the aircraft can produce sufficient thrust in case of a motor failure. The fourth flight condition is

Table 2 – Characteristics of Skyfly Axe-like tilt-wing eVTOL aircraft [55]

Dimensions			
Aircraft length [m]	4.4		
Wing span [m]	5.0		
Wing area [m <sup>2</sup> ]	6.0		
Canard span [m]	5.0		
Canard area [m <sup>2</sup> ]	4.0		
Aerodynamics			
Stall speed [m/s]	21.5		
Cruise speed [m/s]	44.7		
Lift to drag ratio [-]	9		
Mass			
Maximum takeoff mass [kg]	652		

to maximise the thrust margin<sup>2</sup> during hover for maneuverability capability. Table 3 summarises the cruise and hover flight conditions. As shown in Table 3, the thrust requirement at hover is an order of magnitude larger than that at cruise.

Table 3 – Baseline operating conditions

Parameter	Operating conditions		
i didilicici	Cruise	Hover	
Altitude h [m]	500	25	
Air density $ ho_0$ [kg/m $^3$ ]	1.167	1.222	
Air temperature $T_0$ [K]	284.9	288.0	
Flight speed [m/s]	31.3	0.0	
Thrust requirement [N]	711	6,327	

In the optimisation study, we consider four objectives. The first two objectives are to minimise powertrain input power in cruise and hover. Instead of propeller efficiency, we employ powertrain input power as the objective, as it encapsulates the efficiency of both the electric motor and the proprotor. This choice avoids the risk of optimising a proprotor that is mismatched to the electric motor under consideration. The third objective is to maximise the thrust margin during hover. Finally, the fourth objective of the study is to minimise the noise generated by the proprotors during hover operation.

## 4.2 Optimisation Results

This section presents the comparison between the optimisation case with the original and modified motor. We use a population of 16 times the number of design variables (496) and terminate the optimisation once the hypervolume indicator<sup>3</sup> converges.

The Pareto fronts in Figures 5, 6 and 7 show feasible designs across all four objectives and compare the performance of the optimised proprotors with the original and modified motors. Five Pareto-optimal proprotor designs (labelled proprotors A, B, C, D, and E) are chosen from the non-dominated front (solutions coloured in black) in Figures 5, 6 and 7. Proprotor A requires the lowest cruise power, while proprotor B requires the smallest power draw in hover. Proprotor C provides the highest thrust margin, while proprotor D is the quietest proprotor during hover operation. Finally, proprotor E is the

<sup>&</sup>lt;sup>2</sup>The thrust margin is defined as the ratio between the thrust generated at the hover condition to the thrust required to hover.

<sup>&</sup>lt;sup>3</sup>The hypervolume indicator measures the volume of the dominated portion of the objective space.

design that is the closest to the ideal point<sup>4</sup>.

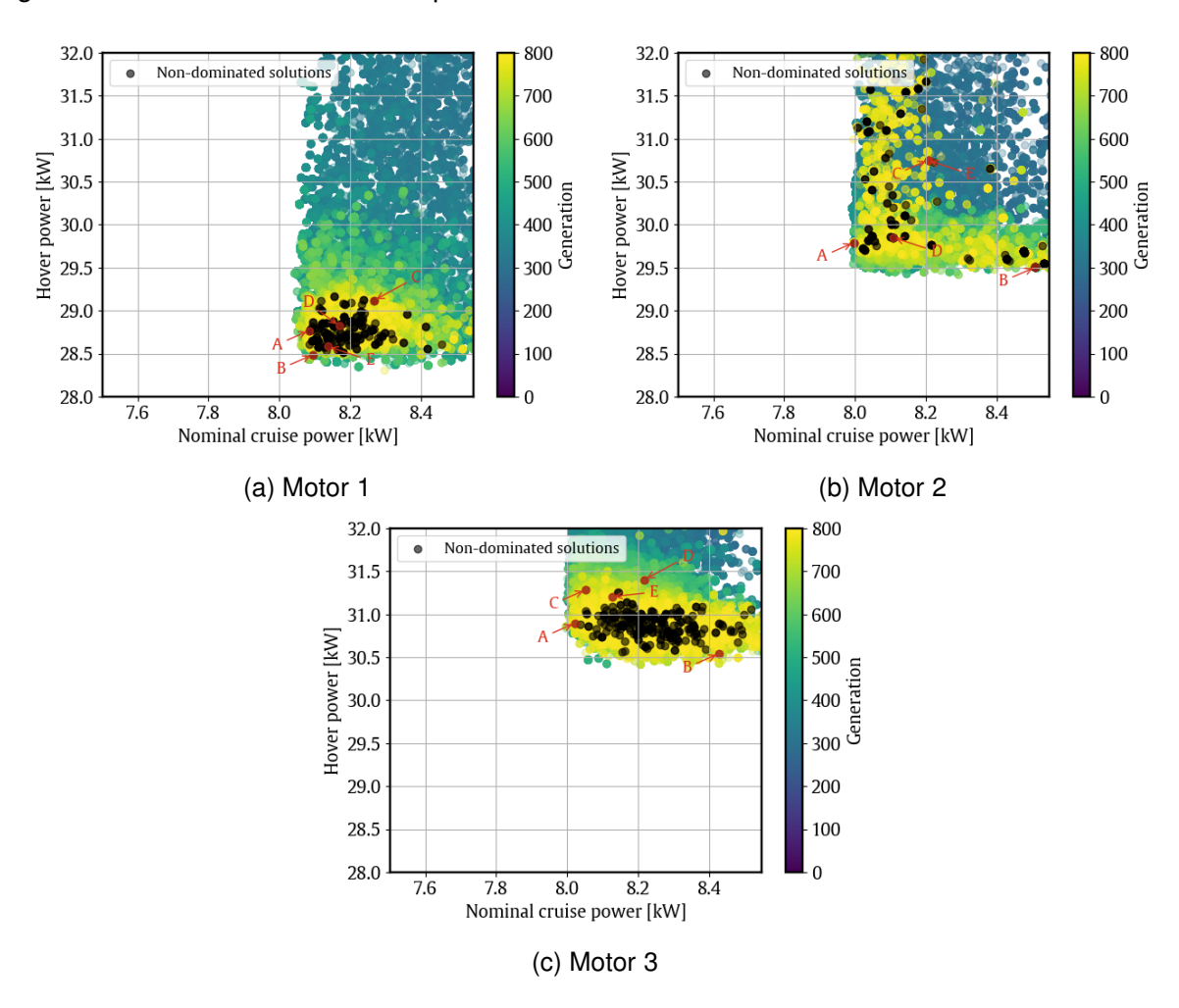


Figure 5 – Evolution history and Pareto fronts showing tradeoff between cruise and hover power

As illustrated in Figures 5, 6, and 7, the performance of Pareto-optimal proprotors is markedly influenced by the electric motor, particularly in hover flight conditions. For the best-compromised proprotor design (proprotor E), optimised with Motors 1, 2 and 3, the hover power is 28.5 kW, 30.9 kW and 31.2 kW, respectively. The thrust margins for the three cases are very close, approximately 1.43, 1.52 and 1.41 for the Motors 1, 2 and 3. Notably, Figure 7 reveals the most significant disparity in hover noise. The hover noise for the proprotor optimised with Motor 1 is 58 dB, whereas for Motors 2 and 3, the hover noise is 50.4 dB and 41 dB, respectively.

Figure 8 shows the operating points of each Pareto-optimal proprotor on their corresponding motor map. For cruise and hover flight conditions, the torque depicted in Figure 8 is half of the total torque, assuming an equal contribution from each of the two motors as two motors are used to run proprotor. However, for the emergency hover flight condition, a single motor must produce all the required torque for the proprotor.

Examining Figure 8, it is evident that the proprotor operates in a high-efficiency region on the motor map for cruise and nominal hover. This shows the significance of including proprotor-to-powertrain matching in the optimisation process, ensuring that proprotors do not operate outside the high-efficiency region on the motor map.

From the hover operating points in Figures 8a, 8b and 8c, the operating rotational speed for the proprotors optimised with the modified motors is slower than that for the original motor. This explains the low hover noise characteristics of the Pareto-optimal proprotors optimised with the modified motors.

<sup>&</sup>lt;sup>4</sup>The ideal point is the point that has the optimum value for all objectives.

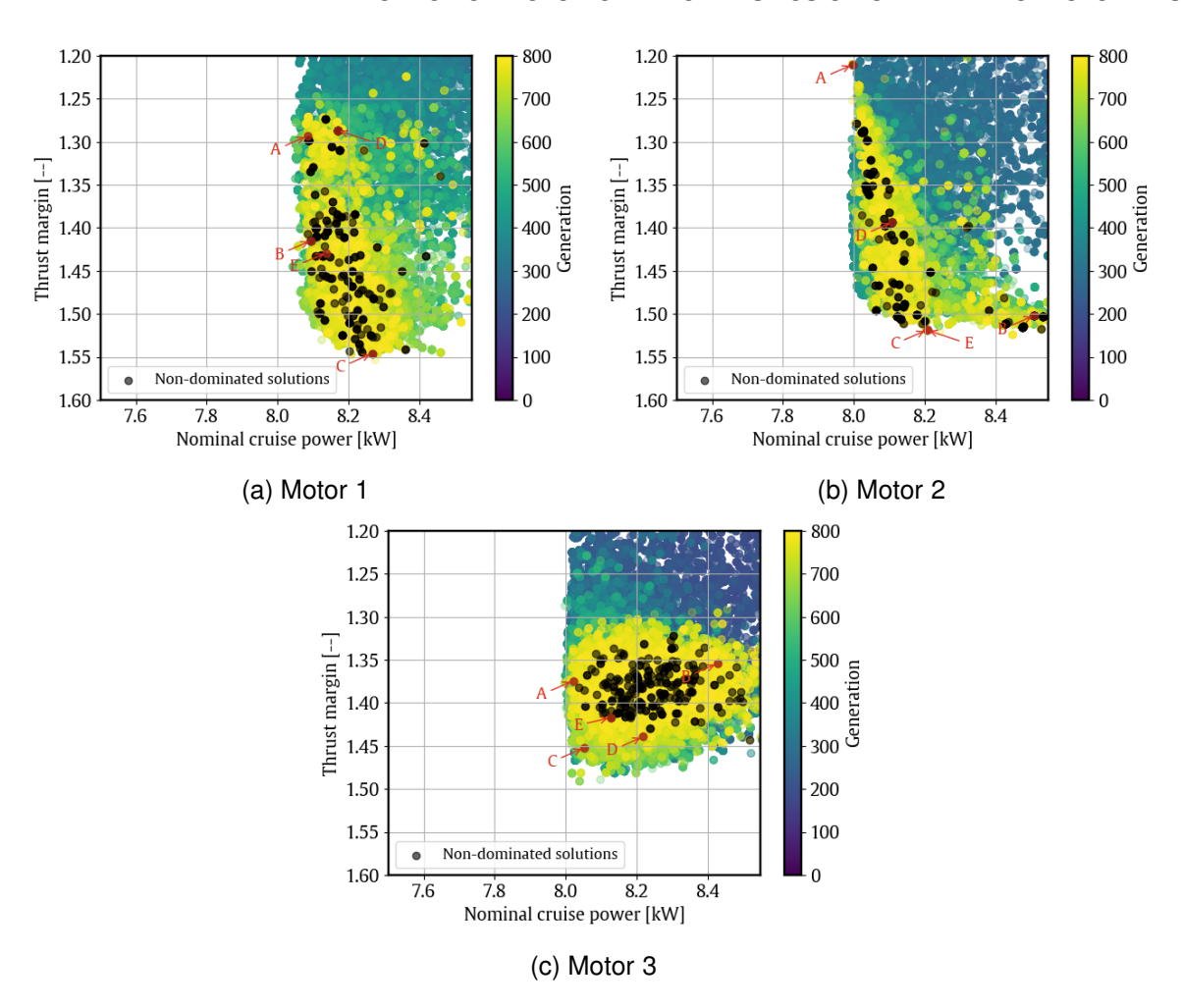


Figure 6 – Evolution history and Pareto fronts showing tradeoff between cruise power and thrust margin

Operating at a lower rotational speed reduces hover noise at the expense of a slightly higher hover power.

Figure 9 compares the distributions of chord length and pitch angle for the Pareto fronts of the three optimisation cases. Notably, the chord length of proprotors optimised with the modified motors is bigger than to those designed with the original motor. This is attributed to the low operating rotational speed of the proprotors optimised with the modified motor. To meet the required thrust during hover, the proprotor blade area needs to increased to compensate for the slower operating rotational speed as the motor can provide higher torque.

Moreover, the pitch angles of the proprotors optimised with the modified motors are larger than those of the original motor. Once again, due to the low rotational speed, an increase in pitch angle is necessary to ensure that each section of the proprotor blade can generate a higher lift which is directly proportional to the thrust generated.

The full geometry of proprotors A, B, C, D, and E for the three optimisation cases is shown in Figures 10, 11 and 12.

## 5. Conclusion

Proprotor optimisation studies frequently neglect the vehicle's powertrain. This study introduces an optimisation framework for proprotors designed for electric vertical takeoff and landing aircraft. It integrates a blade element momentum theory aerodynamic solver with models accounting for electric motors, structural integrity, and acoustic considerations. The design variables include proprotor chord, pitch, and rotation speed, with a set of constraints imposed to ensure the production of viable

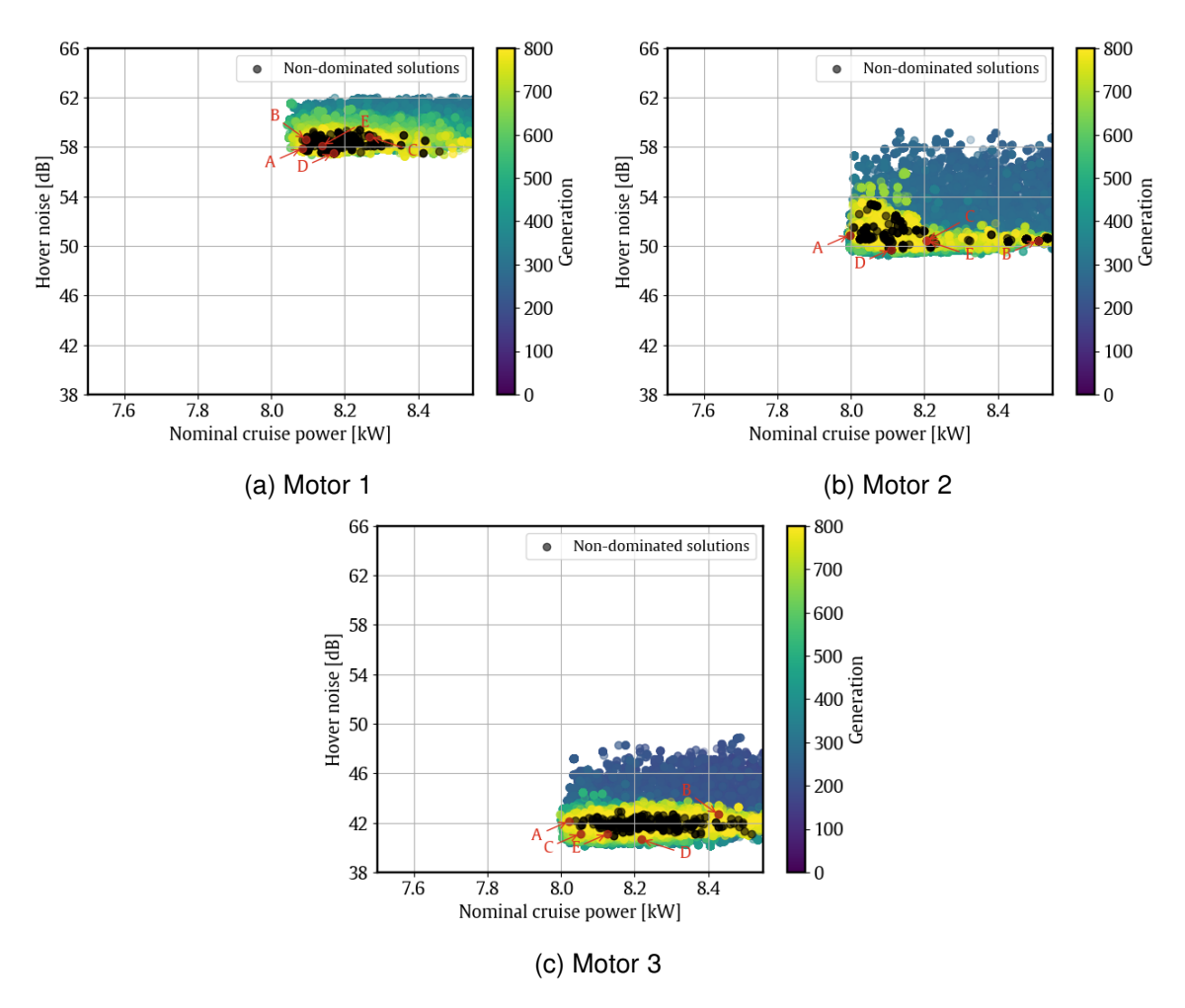


Figure 7 – Evolution history and Pareto fronts showing tradeoff between cruise power and hover noise

proprotor shapes that meet all operational requisites.

Three proprotor optimisation simulations are conducted, each paired with a different electric motor, possessing the same power rating but differing in maximum torque and rotational speed. The results unveil that the Pareto-optimal proprotor designs are significantly influenced by the specific electric motors to which they are coupled. Proprotors designed for motor with higher maximum torque and lower maximum rotational speed require larger chord and pitch distributions in contrast to their counterparts designed for motors with lower maximum torque and higher maximum rotational speed. Additionally, owing to the slower operating rotational speed of the proprotors optimised with higher maximum torque and smaller maximum rotational speed, the noise generated during hover operation is notably reduced at the expense of higher hover power.

## Acknowledgement

This research was funded by the Commonwealth Government of Australia under the Cooperative Research Centres Projects (CRC-P) Grant Scheme. The authors thank AMSL Aero, the lead applicant, for their support. D. Verstraete is supported by the Australian Research Council Future Fellowship (FT230100519), funded by the Australian Government.

## **Contact Author Email Address**

Shahfiq Shahjahan: shahfiq.shahjahan@sydney.edu.au

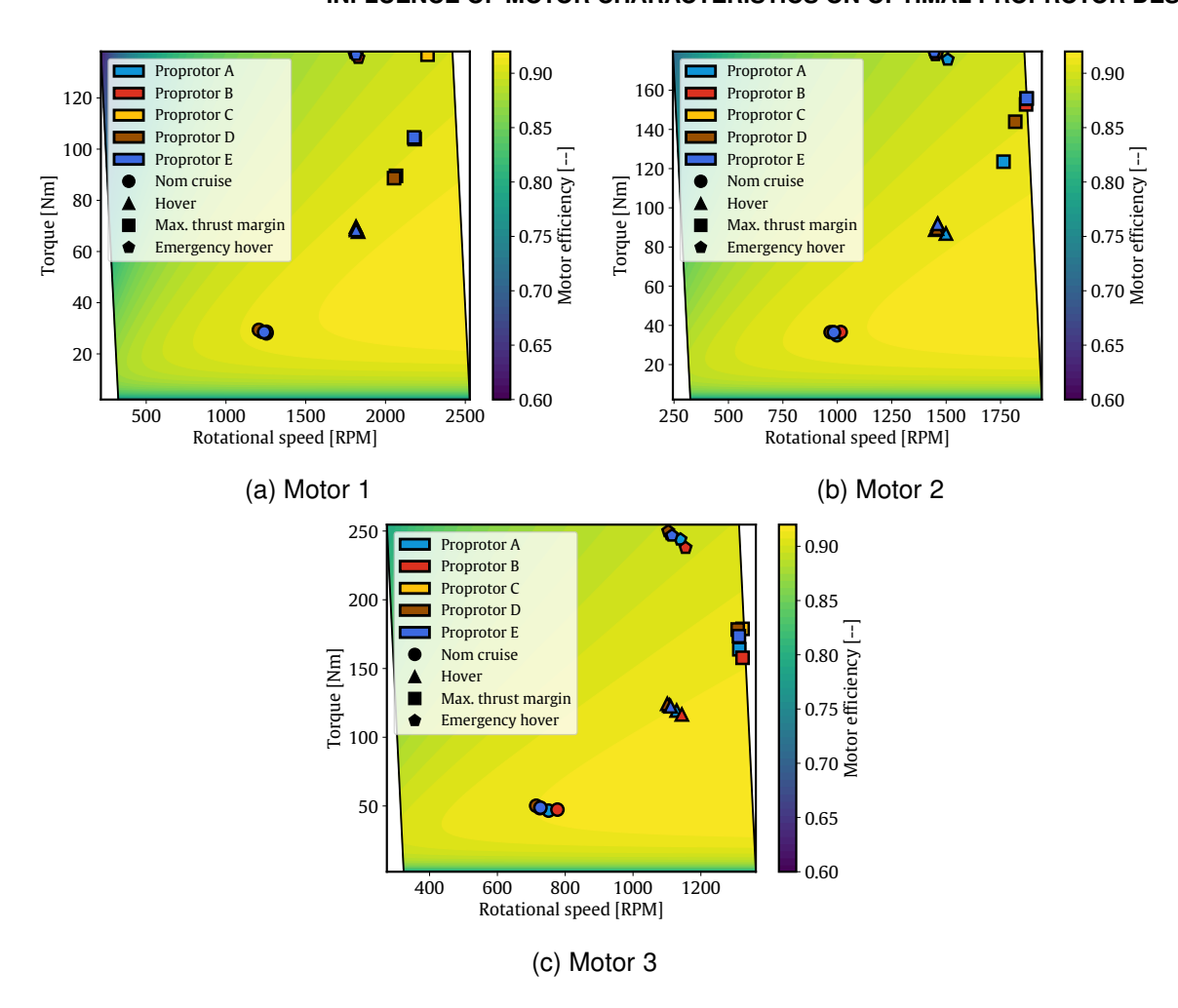


Figure 8 - Operating points of selected Pareto-optimal proprotors on the motor map

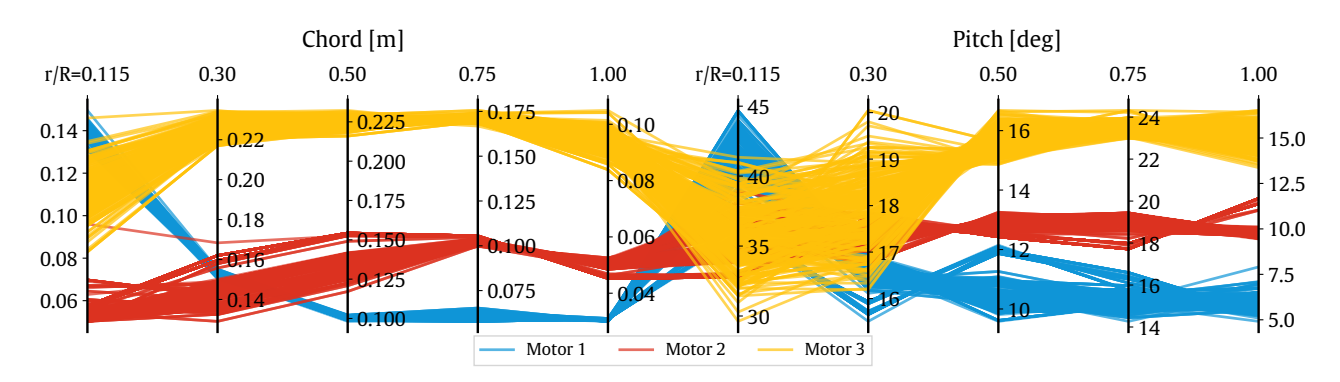


Figure 9 – Parallel coordinates plot showing the difference in the design variables between optimised proprotor with original and modified motor

# **Copyright Statement**

The authors confirm that they, and/or their company or organization, hold copyright on all of the original material included in this paper. The authors also confirm that they have obtained permission, from the copyright holder of any third party material included in this paper, to publish it as part of their paper. The authors confirm that they give permission, or have obtained permission from the copyright holder of this paper, for the publication and distribution of this paper as part of the ICAS proceedings or as individual off-prints from the proceedings.

### References

[1] A. Brown and W. Harris. *A Vehicle Design and Optimization Model for On-Demand Aviation*. AIAA SciTech Forum. American Institute of Aeronautics and Astronautics, 2022/01/11 2018.

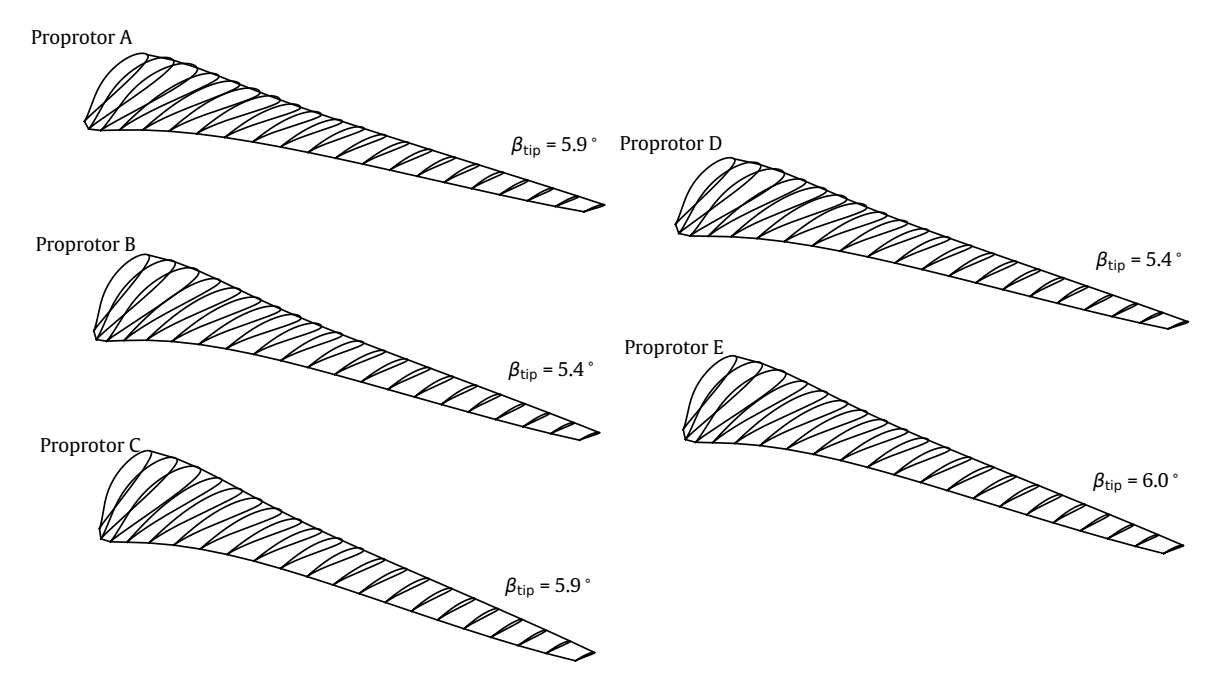


Figure 10 - Geometry of selected Pareto-optimal proprotors with Motor 1

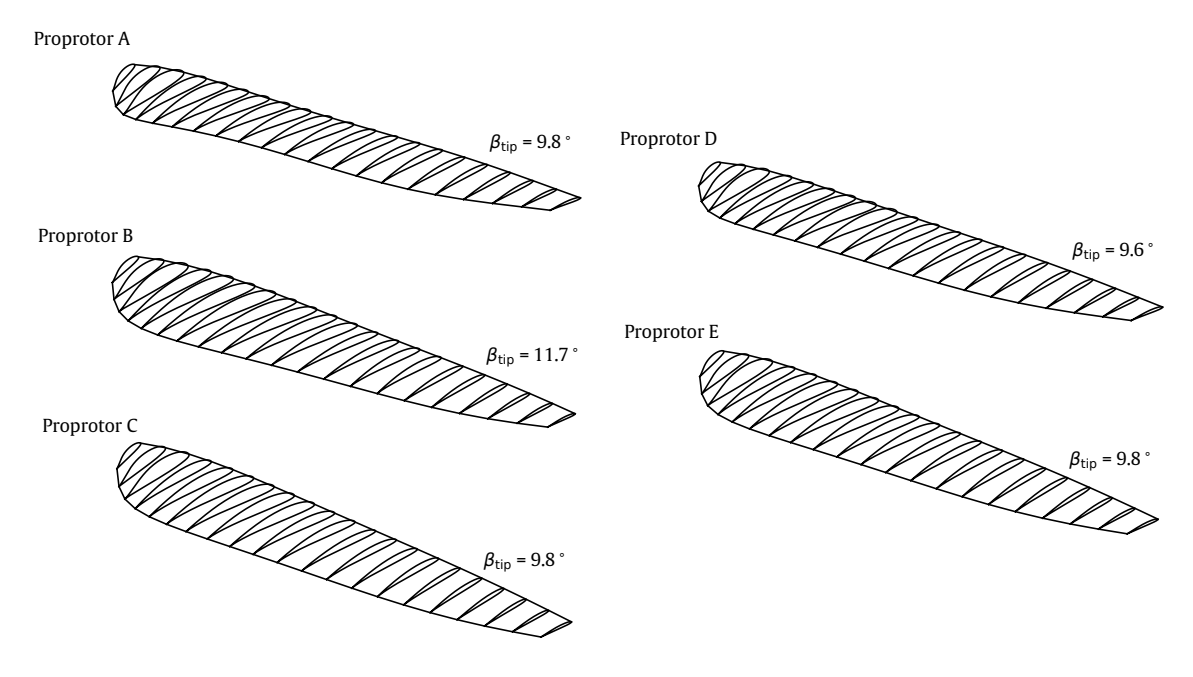


Figure 11 – Geometry of selected Pareto-optimal proprotors with Motor 2

- [2] W. J. Fredericks, M. D. Moore, and R. C. Busan. *Benefits of Hybrid-Electric Propulsion to Achieve 4x Cruise Efficiency for a VTOL UAV.* AIAA AVIATION Forum. American Institute of Aeronautics and Astronautics, 2022/01/11 2013.
- [3] F. Finger. Comparative Performance and Benefit Assessment of VTOL and CTOL UAVs. In *Deutscher Luft-und Raumfahrtkongress (DLRK)*, 2016.
- [4] M. Moore. *NASA Puffin Electric Tailsitter VTOL Concept*. Aviation Technology, Integration, and Operations (ATIO) Conferences. American Institute of Aeronautics and Astronautics, 2022/01/11 2010.
- [5] M. D. Moore. *Misconceptions of Electric Aircraft and their Emerging Aviation Markets*. AIAA SciTech Forum. American Institute of Aeronautics and Astronautics, 2022/01/11 2014.
- [6] W. Johnson, C. Silva, and E. Solis. Concept vehicles for VTOL air taxi operations. In AHS Technical Conference on Aeromechanics Design for Transformative Vertical Flight, San Francisco, CA, January 16-19, 2018, NASA Ames Research Center, Moffett Field, California, 2018.

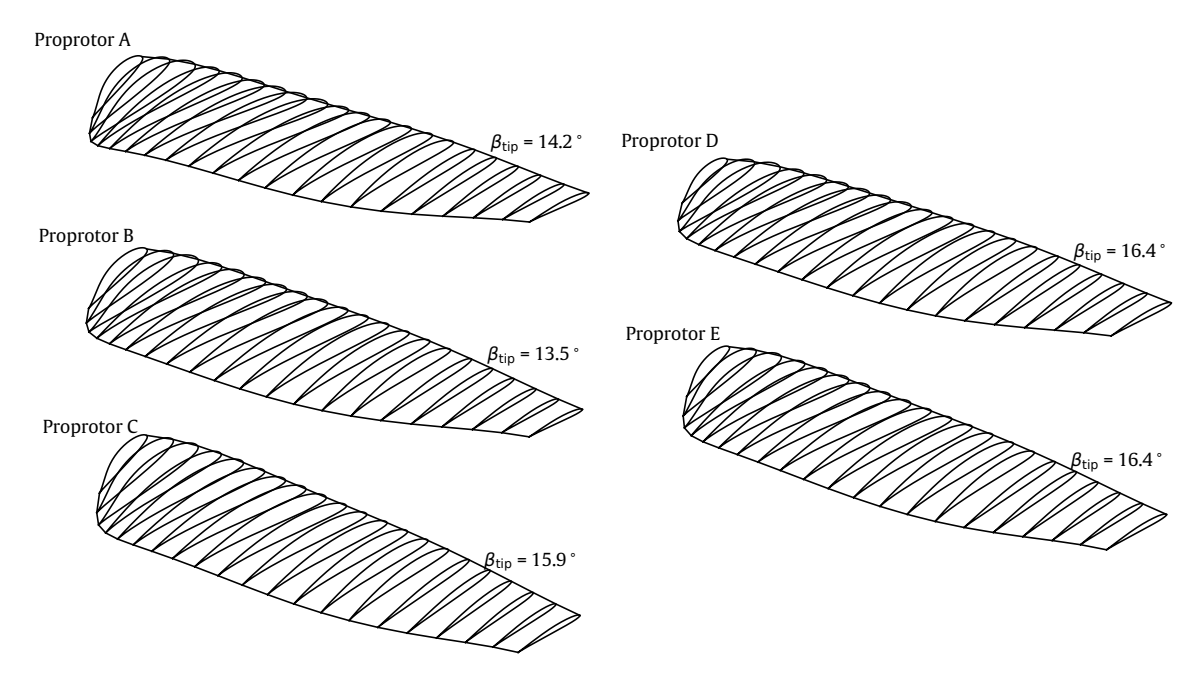


Figure 12 – Geometry of selected Pareto-optimal proprotors with Motor 3

- [7] J. Holden and N. Goel. Fast-forwarding to a future of on-demand urban air transportation. 2016.
- [8] R. Goyal. Urban air mobility (UAM) market study, 2018 (accessed 12.01.2022).
- [9] O. Gur and A. Rosen. Optimizing electric propulsion systems for unmanned aerial vehicles. *Journal of Aircraft*, 46(4):1340–1353, 2021/10/19 2009.
- [10] K. Kim, T. Kim, K. Lee, and S. Kwon. Fuel cell system with Sodium Borohydride as Hydrogen source for unmanned aerial vehicles. *Journal of Power Sources*, 196(21):9069–9075, 2011.
- [11] D. Verstraete, L. Cazzato, and G. Romeo. Preliminary design of a fuel-cell-based hybrid-electrical UAV. In 28th International Congress of the Aeronautical Sciences, volume 1, pages 422–431. ICAS-2012-654, September 2012.
- [12] K. Lehmkuehler, KC. Wong, and D. Verstraete. Design and test of a UAV blended wing body configuration. In 28th International Congress of the Aeronautical Science. ICAS-2012-675, September 2012.
- [13] D. Verstraete. Multi-disciplinary optimisation of medium altitude long endurance UAVs. In *31st International Congress of the Aeronautical Science*. ICAS-2018-416, 2018.
- [14] D. Verstraete, J. L. Palmer, and M. Hornung. Preliminary sizing correlations for fixed-wing unmanned aerial vehicle characteristics. *Journal of Aircraft*, 55(2):715–726, 2018.
- [15] K. G. Nikolakopoulos, K. Soura, I. K. Koukouvelas, and N. G. Argyropoulos. UAV vs classical aerial photogrammetry for archaeological studies. *Journal of Archaeological Science: Reports*, 14:758–773, 2017.
- [16] C. Zhang and J. M. Kovacs. The application of small unmanned aerial systems for precision agriculture: a review. *Precision Agriculture*, 13(6):693–712, 2012.
- [17] C. Gomez and H. Purdie. UAV-based photogrammetry and geocomputing for hazards and disaster risk monitoring A Review. *Geoenvironmental Disasters*, 3(1):23, 2016.
- [18] D. Giordan, Y. Hayakawa, F. Nex, F. Remondino, and P. Tarolli. Review article: the use of remotely piloted aircraft systems (RPASs) for natural hazards monitoring and management. *Nat. Hazards Earth Syst. Sci.*, 18(4):1079–1096, 2018. NHESS.
- [19] A. Bacchini and E. Cestino. Electric VTOL Configurations Comparison. Aerospace, 6(3), 2019.
- [20] C. Silva, W. R. Johnson, E. Solis, M. D. Patterson, and K. R. Antcliff. VTOL urban air mobility concept vehicles for technology development. In *2018 Aviation Technology, Integration, and Operations Conference*. American Institute of Aeronautics and Astronautics, 2021/10/19 2018.

- [21] A. Bacchini, E. Cestino, B. Van Magill, and D. Verstraete. Impact of lift propeller drag on the performance of eVTOL lift+cruise aircraft. Aerospace Science and Technology, 109:106429, 2021.
- [22] O. Gur and G. Lazar. Prop-rotor design for an electric tilt-rotor vehicle. In *American Helicopter Society Future Vertical Lift Aircraft Design Conference*, 2012.
- [23] Paul E. I. Pounds and Robert E. Mahony. Small-scale Aeroelastic Rotor Simulation, Design and Fabrication. Proceedings of the 2005 Australasian Conference on Robotics and Automation, 2005.
- [24] Jurij Sodja, Domen Stadler, and Tadej Kosel. Computational Fluid Dynamics Analysis of an Optimized Load-Distribution Propeller. *Journal of Aircraft*, 49(3):955–961, 2012.
- [25] Jurij Sodja, Radovan Drazumeric, Tadej Kosel, and Pier Marzocca. Design of Flexible Propellers with Optimized Load-Distribution Characteristics. *Journal of Aircraft*, 51(1):117–128, 2014.
- [26] R. MacNeill and D. Verstraete. Optimal Propellers for a Small Hybrid Electric Fuel-Cell UAS. In 2018 AIAA/IEEE Electric Aircraft Technologies Symposium, AIAA Propulsion and Energy Forum. American Institute of Aeronautics and Astronautics, 2022/02/07 2018.
- [27] O. Gur and A. Rosen. Optimization of propeller based propulsion system. *Journal of Aircraft*, 46(1):95–106, 2021/10/19 2009.
- [28] X. Geng, P. Liu, T. Hu, Q. Qu, J. Dai, C. Lyu, Y. Ge, and R. A. D. Akkermans. Multi-fidelity optimization of a quiet propeller based on deep deterministic policy gradient and transfer learning. *Aerospace Science and Technology*, 137:108288, 2023.
- [29] H. H. Mian, G. Wang, H. Zhou, and X. Wu. Optimization of thin electric propeller using physics-based surrogate model with space mapping. Aerospace Science and Technology, 111:106563, 2021.
- [30] R. MacNeill and D. Verstraete. Propeller optimisation for an electrically-powered tactical UAS. In *International Council of the Aeronautical Sciences, ICAS 2018*, AIAA Propulsion and Energy Forum. American Institute of Aeronautics and Astronautics, 2022/02/07 2018.
- [31] S. Shahjahan, A. Gong, A. Moore, and D. Verstraete. Optimisation of proprotors for tilt-wing eVTOL aircraft. Aerospace Science and Technology, 144:108835, 2024.
- [32] R. MacNeill and D. Verstraete. Blade element momentum theory extended to model low Reynolds number propeller performance. *The Aeronautical Journal*, 121(1240):835–857, 2017.
- [33] L. A. Viterna and R. D. Corrigan. Fixed Pitch Rotor Performance of Large Horizontal Axis Wind Turbines. Technical report, NASA Lewis Research Venter, Cleveland, Ohio, USA, 1982.
- [34] H. Snel, R. Houwini, and J. Bosschers. Sectional prediction of lift coefficients on rotating wind turbine blades in stall. Technical Report ECN-C-93-052, National Aerospace Laboratory (NLR), Amsterdam, Netherlands, 1994.
- [35] M. Drela. XFOIL: An analysis and design system for low Reynolds number airfoils, pages 1–12. 1989.
- [36] J.B Brandt, R.W Deters, G.K Ananda, O.D Dantsker, and M.S Selig. UIUC Propeller Database, 2020 (accessed 12.01.2022).
- [37] H. Rosenstein and R. Clark. Aerodynamic development of the V-22 tilt rotor. Aircraft Design and Technology Meeting. American Institute of Aeronautics and Astronautics, 2022/01/12 1986.
- [38] J. P. Rabbott. Static-Thrust Measurements of the Aerodynamic Loading on a Helicopter Rotor Blade. Technical report, Langley Aeronautical Laboratory, Langley Field, Va, 1956.
- [39] J. G. Leishman. *Principles of helicopter aerodynamics*. Cambridge University Press, New York, 2nd edition edition, 2006.
- [40] J.M. Drees. A Theory of Airflow through rotors and its application to some harmonic problems. The Journal of the Helicopter Association of Great Britain, 3(2):79–104, 1949.
- [41] D. Serrano, M. Ren, A. J. Qureshi, and S. Ghaemi. Effect of disk angle-of-attack on aerodynamic performance of small propellers. Aerospace Science and Technology, 92:901–914, 2019.

- [42] A. F. Deming. Noise from Propellers with Symmetrical Sections at Zero Blade Angle, II. Technical report, National Advisory Committee for Aeronautics, 1938.
- [43] L. Gutin. On the Sound Field of a Rotating Propeller. Technical report, National Advisory Committee for Aeronautics, Langley Aeronautical Laboratory, Langley Field, VA, 1948.
- [44] P. J. A Minguet. Static and Dynamic Behavior Composite of Helicopter Rotor Blades under Large Deflections. PhD thesis, Massachusetts Institute of Technology, 1989.
- [45] R. MacNeill and D. Verstraete. Validation of an Aeroelastic Rotor Analysis Method. In *2018 Joint Propulsion Conference*, AIAA Propulsion and Energy Forum. American Institute of Aeronautics and Astronautics, 2022/02/07 2018.
- [46] Hexcel. HexTow Continuous Carbon Fiber, 2022 (accessed: 12.01.2022).
- [47] Hexcel. HexTow AS4 Carbon Fiber, 2022 (accessed: 12.01.2022).
- [48] Hexcel. 3501-6 Epoxy Matrix, 2022 (accessed: 12.01.2022).
- [49] E. J Barbero. Introduction to Composite Materials Design. CRC Press, second edition edition, 2011.
- [50] Evonik. Product Information: ROHACELL HERO, 2022 (accessed: 12.01.2022).
- [51] G. Kreisselmeier and R. Steinhauser. Systematic Control Design by Optimizing a Vector Performance Index. *IFAC Proceedings Volumes*, 12(7):113–117, 1979.
- [52] M. Drela. First-Order DC Electric Motor Model. Technical report, Massachusetts Institute of Technology, 2007.
- [53] Geiger Engineering. Complete electric drive system, 2023 (accessed: 09.12.2023).
- [54] M. Hepperle. Aerodynamics of Model Aircraft, 2018 (accessed: 15.02.2022).
- [55] Skyfly. Skyfly Axe eVTOL Technical Specification, 2023 (accessed 09.12.2023).
- [56] N. Panagant, S. Bureerat, and K. Tai. A novel self-adaptive hybrid multi-objective meta-heuristic for reliability design of trusses with simultaneous topology, shape and sizing optimisation design variables. *Structural and Multidisciplinary Optimization*, 60(5):1937–1955, 2019.
- [57] K. Deb and H. Jain. An Evolutionary Many-Objective Optimization Algorithm Using Reference-Point-Based Nondominated Sorting Approach, Part I: Solving Problems With Box Constraints. *IEEE Transactions on Evolutionary Computation*, 18(4):577–601, 2014.
- [58] H. Jain and K. Deb. An Evolutionary Many-Objective Optimization Algorithm Using Reference-Point Based Nondominated Sorting Approach, Part II: Handling Constraints and Extending to an Adaptive Approach. *IEEE Transactions on Evolutionary Computation*, 18(4):602–622, 2014.